Electronic structure and x-ray magnetic circular dichroism in the multiferroic oxide *h*-$YbFeO_3$

V. N. Antonov[1,2] and D. A. Kukusta[1,3]
[1]*G. V. Kurdyumov Institute for Metal Physics of the N.A.S. of Ukraine, 36 Vernadsky Street, 03142 Kiev, Ukraine*
[2]*Faculty of Mathematics and Informatics, University of Bialystok, K. Ciolkowskiego 1M, PL-15-245 Bialystok, Poland*
[3]*Max-Planck-Institut für Festkörperforschung, Heisenberg Strasse 1, D-70569 Stuttgart, Germany*

(Received 28 December 2018; published 4 March 2019)

Hexagonal ferrites (*h*-$RFeO_3$, $R =$ Sc, Y, Ho-Lu) have recently been identified as a new family of multiferroic complex oxides. We study electronic and magnetic properties of *h*-$YbFeO_3$ ferrite within the density-functional theory using the generalized gradient approximation (GGA) with consideration of strong Coulomb correlations (GGA+U) in the framework of the fully relativistic spin-polarized Dirac linear muffin-tin orbital band-structure method. The $4f$ electrons of Yb are explicitly treated as valence electrons. The x-ray absorption spectra and x-ray magnetic circular dichroism (XMCD) at the Yb $M_{4,5}$, Fe $L_{2,3}$, and O K edges were investigated theoretically. The calculated results are in good agreement with experimental data. We found that the GGA+U approach with Hubbard $U_{\mathrm{eff}} = 6.1$ eV and 3.3 eV for Yb and Fe, respectively, well describes the XMCD spectra at the Yb $M_{4,5}$, Fe $L_{2,3}$, and O K edges.

DOI: 10.1103/PhysRevB.99.104403

I. INTRODUCTION

Multiferroics (MFs) are compounds where long-range magnetic and electric dipolar orders coexist [1]. There is plenty of fascinating physics in these materials, owing to the strong entanglement of spin-charge-orbital degrees of freedom [2,3] and great potential for technological applications in energy-efficient information processing and storage [4–6]. For widespread implementation of new technology, the coexistence of long-range magnetic and electric orders at room temperature will be required; at present, there is only one material, $BiFeO_3$, known to exhibit ferroelectric and antiferromagnetic (AFM) orders above room temperature [7]. Recently, several manganese and iron oxides have been shown to possess strong coupling, promising for realizing room-temperature multiferroic materials. However, ferroelectricity in these materials is rather weak [8].

Rare-earth (RE) orthoferrites exhibit two orders of magnitude faster spin dynamics in comparison to conventional ferromagnetic (FM) materials [9,10]. Magnetic property investigations of the RE orthoferrites $RFeO_3$ have shown that the Fe^{3+} moments are ordered in a canted AFM structure Γ_4 at high temperature with $T_N \approx 600$ K (details of the notations are given in Ref. [11]), and the spin canting gives a weak net ferromagnetic moment along the c axis [11–13]. With decreasing temperature, a spontaneous spin-reorientation transition from the Γ_4 to the Γ_2 magnetic configuration occurs in many orthoferrites with magnetic R ions in a wide temperature range from $T_{\mathrm{SR}} \approx 450$ K for $SmFeO_3$ down to $T_{\mathrm{SR}} \approx 7.6$ K for $YbFeO_3$, and the net magnetic moment rotates from the a to the c axis [11,12].

The RE orthoferrites $RFeO_3$ have either orthorhombic or hexagonal phases. Orthorhombic $RFeO_3$ (o-$RFeO_3$) with the centrosymmetric perovskite structure (space group *Pnma*) is the thermodynamically stable phase [14,15] and is known to be paraelectric. On the other hand, hexagonal $RFeO_3$ (*h*-$RFeO_3$) with the $P6_3cm$ space group exists as a metastable phase. The structure of *h*-$RFeO_3$ is unique in the following regards: the c axis in the unit cell is laminated by RE and Fe layers, and the Fe ions have a trigonal bipyramidal coordination [16]. Such characteristics are not seen in the perovskite structure. Thus the structure of the *h*-$RFeO_3$ phase could exhibit unique physical properties. However, there are only a few studies on the practical applications of *h*-$RFeO_3$ [17–19] because it is difficult to synthesize *h*-$RFeO_3$ using conventional methods, such as the co-precipitation method [20], and because metastable *h*-$RFeO_3$ is easily transformed into thermodynamically stable o-$RFeO_3$.

Hexagonal ferrites *h*-$RFeO_3$ ($R =$ Sc, Y, and Ho-Lu) are expected to be ferroelectric due to the polar structure that lies at the origin of the ferroelectricity of $YMnO_3$ above room temperature ($T_C \sim 1000$ K) [21]. Antiferromagnetic spin structures involving a triangular arrangement of the moments in the a-b plane are expected in *h*-$RFeO_3$ due to the structural symmetry [22]. Despite the frustration created by the triangular lattice, the strong interactions between the Fe^{3+} sites due to high spin and large Fe-O interactions [23] are expected to greatly increase the magnetic ordering temperature of *h*-$RFeO_3$ compared with that of $RMnO_3$ ($T_N \sim 100$ K) [24]. This makes *h*-$RFeO_3$ promising candidates to be room-temperature multiferroics. In fact, the evidence of ferroelectricity has been found in the *h*-$YbFeO_3$ films below 470 K [25,26].

A landmark on the understanding of this complex magnetic systems was established by White in his well known review paper in 1969 [11]. Up to now, comparing to lots of experiment observations, there are only a few theoretical reports on $RFeO_3$ family. Using first-principles calculations, Iglesias *et al.* [27] and Xing *et al.* [28] identified that the antiferromagnetic structures between Fe $3p$ moments are

2469-9950/2019/99(10)/104403(10)

energetically favored in almost all cases except for $SmFeO_3$. Afterwards, Adams and Amadon studied the magnetic properties of $LuFeO_3$ under high-pressure conditions and found that $LuFeO_3$ would exhibit large volume transitions associated with a spin collapse [29]. With different density functional theory (DFT) computational schemes, Stroppa *et al.* [8] confirmed that the ferroelectric polarization in $DyFeO_3$ is driven by an exchange-striction mechanism, the authors further stated that the coupling between Dy and Fe spin sublattices is mediated by Dy 5*d* and O 2*p* hybridization.

Recently, Nikitin *et al.* [30] present the study of the spin dynamics in $YbFeO_3$ at temperatures close to the SR transition and in magnetic fields applied along three crystallographic directions. Using inelastic neutron scattering, they observed two collective modes in the spectrum of magnetic excitations well separated in energy: 3D gapped magnons, associated with the AFM ordered Fe subsystem, and quasi-1D AFM fluctuations within the Yb subsystem, with no hybridization of those two modes. They show that a weak quasi-1D coupling within the Yb subsystem $J_{\text{Yb-Yb}}$ creates unusual quantum spin dynamics on the low-energy scales. At $T < T_{\text{SR}}$, the Yb spin chains have a well defined field-induced ferromagnetic ground state, whereas at $T > T_{\text{SR}}$ the Yb excitation spectrum shows the coexisting of spinon and magnon modes.

In the present study, we focus our attention on the theoretical investigation of the x-ray linear dichroism (XLD) and x-ray magnetic circular dichroism (XMCD) in the *h*-$YbFeO_3$ compound from first principles. The XMCD experiments measure the difference of the absorption of x-rays with opposite (left and right) directions of circular polarization. The XMCD is a powerful tool to study the element-specific local magnetic interactions and also it reflects the spin and orbital polarizations of the local electronic states. The x-ray absorption spectra (XAS) and XMCD at the Yb $M_{4,5}$, Fe $L_{2,3}$, and O *K* edges in the *h*-$YbFeO_3$ were measured by Cao *et al.* [31]. From the temperature and magnetic-field dependence of the Yb magnetization, they found that the low-temperature Yb magnetic moment is significantly reduced compared with the value of free Yb^{3+} ions, indicating the effect of the crystal field. The exchange field on Yb, generated by the Fe moments, tends to antialign the magnetization of Fe and Yb at low temperature. They also investigated possible valence mixing of Yb and only found an indication of Yb^{2+} at the surface of samples grown in an Ar environment, suggesting an insignificant effect on the bulk magnetism of the *h*-$YbFeO_3$ studied in this work.

Here we present comprehensive theoretical calculations of the electronic structure as well as XAS and XMCD spectra of the *h*-$YbFeO_3$. The energy band structure of the *h*-$YbFeO_3$ in this paper is calculated within the *ab initio* approach by applying the generalized gradient approximation (GGA) with taking into account strong Coulomb correlations (GGA+*U*) in the frame of the fully relativistic spin-polarized Dirac linear muffin-tin orbital band-structure method. The paper is organized as follows. The computational details are presented in Sec. II. Section III presents the electronic structure of the *h*-$YbFeO_3$ compound. Section IV is devoted to the XAS and XMCD spectra of the *h*-$YbFeO_3$ compound. Theoretical results are compared with experimental measurements. Finally, the results are summarized in Sec. V.

II. COMPUTATIONAL DETAILS

a. Crystal structure. Hexagonal *h*-$YbFe_3$ is a member of hexagonal rare-earth ferrites (*h*-RFe_3, $R =$ Ho-Lu, Y, and Sc). Hexagonal *h*-$YbFe_3$ have a layered crystal structure in which both RE and Fe atoms adopt a two-dimensional triangular lattice [16]. Below about 1000 K, the *h*-$YbFe_3$ crystal structure undergoes a distortion, corresponding to a rotation of the FeO_5 local structure and a buckling of the rare-earth layer, which induces improper ferroelectricity [21,31–33]. The rotation of FeO_5 also cants the moment on Fe, via the Dzyaloshinskii-Moriya (DM) interaction, generating weak ferromagnetism along the *c* direction on top of a 120° antiferromagnetic order in the *a*-*b* plane below 120 K [31,34,35].

The crystal structure of the *h*-$YbFeO_3$ is illustrated in Fig. 1. At room temperature, it belongs to a $P6_3cm$ space group with a sixfold rotational symmetry and lattice constants $a = 6.0728$ Å and $c = 11.7450$ Å [36]. The unit cell can be divided into four layers: two YbO_2 layers and two FeO layers. The arrangements of the atoms follow roughly the ABC hexagonal stacking. The Fe atoms occupy the two-dimensional triangular lattice in the FeO layer. Every Fe atom is surrounded by five oxygen atoms (three in the same FeO layer, one above, and one below the FeO layer), forming a FeO_5 trigonal bipyramid. The hexagonal structure contains two crystallographically independent Yb ions labeled as Yb_1 and Yb_2. Each Yb atom is surrounded by eight oxygen atoms (six in the same RO_2 layer, one above and one below the RO_2 layer), forming a RO_8 local environment. The Yb and Fe ions form the triangular lattice layers, respectively. These trigonal bipyramid layers alternately stack along the *c* axis. The bond lengths between the Fe and O atoms are distributed at 1.8202, 1.9762, 2.0351, and 2.0488 Å in the FeO_5 trigonal bipyramid. The Yb_1-O_3 distance, 2.3482 Å, is shorter than the Yb_2-O_4

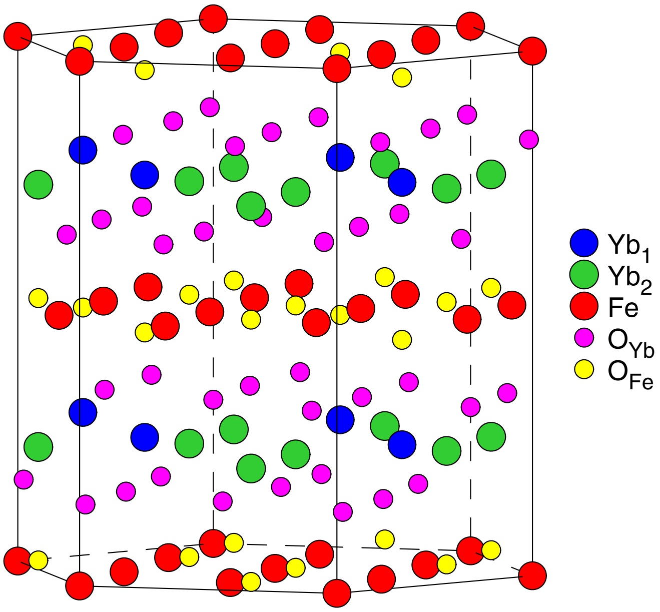

FIG. 1. Crystal structure of the hexagonal *h*-$YbeO_3$ (the space group is $P6_3cm$ No. 185). Red spheres represent Fe atoms, blue and green spheres show Yb atoms, magenta and yellow spheres represent oxygen atoms.

distance, 2.5393 Å in the so-called polar direction along the c axis, which enables us to expect a stronger chemical bonding between the Yb_1 and O_3 atoms. Note that the FeO_5 is slightly rotated along the [120] crystal axis. This rotation causes the broken inversion symmetry of the h-YbeO_3 structure, allowing for the ferroelectricity [21,34,37].

b. X-ray magnetic circular dichroism. Magneto-optical (MO) effects refer to various changes in the polarization state of light upon interaction with materials possessing a net magnetic moment, including rotation of the plane of linearly polarized light (Faraday, Kerr rotation) and the complementary differential absorption of left and right circularly polarized light (circular dichroism). In the near visible spectral range, these effects result from excitation of electrons in the conduction band. Near x-ray absorption edges, or resonances, magneto-optical effects can be enhanced by transitions from well-defined atomic core levels to transition symmetry selected valence states.

Within the one-particle approximation, the absorption coefficient $\mu_j^\lambda(\omega)$ for incident x-ray polarization λ and photon energy $\hbar\omega$ can be determined as the probability of electronic transitions from initial core states with the total angular momentum j to final unoccupied Bloch states

$$\mu_j^\lambda(\omega) = \sum_{m_j}\sum_{n\mathbf{k}} |\langle\Psi_{n\mathbf{k}}|\Pi_\lambda|\Psi_{jm_j}\rangle|^2\delta\big(E_{n\mathbf{k}} - E_{jm_j} - \hbar\omega\big) \times\theta(E_{n\mathbf{k}} - E_F)\,, \tag{1}$$

where Ψ_{jm_j} and E_{jm_j} are the wave function and the energy of a core state with the projection of the total angular momentum m_j; $\Psi_{n\mathbf{k}}$ and $E_{n\mathbf{k}}$ are the wave function and the energy of a valence state in the nth band with the wave vector $\mathbf{k}$; E_F is the Fermi energy.

Π_λ is the electron-photon interaction operator in the dipole approximation

$$\Pi_\lambda = -e\boldsymbol{\alpha}\mathbf{a}_\lambda, \tag{2}$$

where $\boldsymbol{\alpha}$ are the Dirac matrices and $\mathbf{a}_\lambda$ is the λ polarization unit vector of the photon vector potential, with $a_\pm = 1/\sqrt{2}(1, \pm i, 0)$, $a_\parallel = (0, 0, 1)$. Here, $+$ and $-$ denotes, respectively, left and right circular photon polarizations with respect to the magnetization direction in the solid. Then, x-ray magnetic circular and linear dichroism are given by $\mu_+ - \mu_-$ and $\mu_\parallel - (\mu_+ + \mu_-)/2$, respectively. More detailed expressions of the matrix elements in the electric dipole approximation may be found in Refs. [38–40]. The matrix elements due to magnetic dipole and electric quadrupole corrections are presented in Ref. [40].

c. Calculation details. The details of the computational method are described in our previous papers [41–43] and here we only mention several aspects. Band-structure calculations were performed using the fully relativistic linear muffin-tin orbital (LMTO) method [39,44]. This implementation of the LMTO method uses four-component basis functions constructed by solving the Dirac equation inside an atomic sphere [45]. The exchange-correlation functional of a GGA-type was used in the version of Perdew, Burke, and Ernzerhof (PBE) [46]. Brillouin zone (BZ) integration was performed using the improved tetrahedron method [47]. The basis consisted of Yb and Fe s, p, d, and f and O s, p, and d LMTO's.

To take into account electron-electron correlation effects, we used the "relativistic" generalization of the rotationally invariant version of the LSDA+U method [48], which takes into account SO coupling so that the occupation matrix of localized electrons becomes nondiagonal in spin indexes. This method is described in detail in our previous paper [48] including the procedure to calculate the screened Coulomb U and exchange J integrals, as well as the Slater integrals F^2, F^4, and F^6.

The screened Coulomb U and exchange Hund coupling J_H integrals enter the LSDA+U energy functional as an external parameters and have to be determined independently. These parameters can be determined from supercell LSDA calculations using Slater's transition state technique [49,50], from constrained LSDA calculations (cLSDA) [50–54] or from the constrained random-phase approximation (cRPA) scheme [55]. Subsequently, a combined cLSDA and cRPA method was also proposed [56]. The cLSDA calculations produce $J_H = 0.9$ and 0.7 eV for the Yb and Fe sites, respectively, in YbFeO_3. It is known, that the cRPA method underestimates values of U in some cases [57]. On the other hand, the cLSDA method produces too large values of U [58]. Therefore, in our calculations, we treated the Hubbard U as an external parameter and varied it from 5.0 to 9.0 eV and between 3 and 5 eV for Yb and Fe, respectively. We adjusted the value of U to achieve the best agreement with the experiment. We found that the value of $U_{\mathrm{eff}} = U - J_H = 6.1$ and 3.3 eV for Yb and Fe, respectively, gives the best agreement between the calculated and experimental XMCD spectra in YbFeO_3. Our calculations can be considered as the calculations from first prinicples with one additional parameter U_{eff}.

The x-ray absorption and dichroism spectra were calculated taking into account the exchange splitting of core levels. The finite lifetime of a core hole was accounted for by folding the spectra with a Lorentzian. The widths of core levels $\Gamma_{M_{4,5}}$ for Yb, $\Gamma_{L_{2,3}}$ for Fe, and Γ_K for O were taken from Ref. [59]. The finite experimental resolution of the spectrometer was accounted for by a Gaussian of width 0.6 eV.

III. ELECTRONIC AND MAGNETIC STRUCTURES

There are several neutron-scattering measurements devoted to the magnetic structure of hexagonal $R\mathrm{FeO}_3$ oxide [25,32,60,61]. According to those studies, the strongest magnetic interaction between the Fe sites is expected to be the exchange interaction within the FeO layer. Due to the two-dimensional triangular lattice and the antiferromagnetic nature, this in-plane interaction is frustrated if the spins are along the c axis. On the other hand, if the spins are within the FeO plane, the frustration is lifted, generating the so-called 120° orders, where the Fe moments lie within a layer and neighboring Fe moments in a layer are aligned by 120° different directions. Figure 2 summarizes the possible magnetic structures with the propagation vector $\mathrm{K} = (0, 0, 0)$ in the h-YbFeO_3, where Γ_1, Γ_2, Γ_3, and Γ_4 are irreducible representations of the $P6_3cm$ group [37]. For h-$R\mathrm{FeO}_3$, the spins follow one of the orders in Γ_1 to Γ_4 or their combinations. The only irreducible representation that allows for a ferromagnetic component along the c axis is Γ_2 [22]. We notice that Γ_2 cannot be mixed with Γ_4 because it generates uneven spins

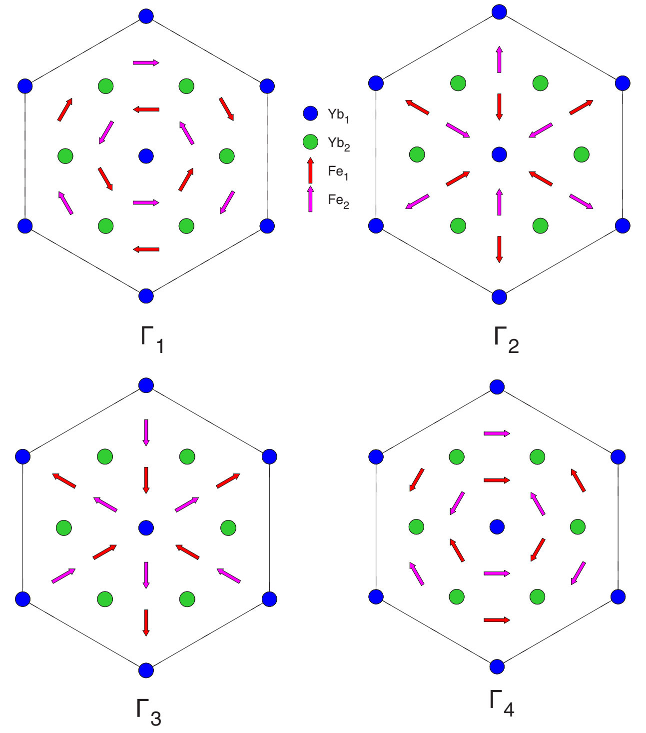

FIG. 2. Four (Γ_1 to Γ_4) independent 120° antiferromagnetic orders of the spins on the Fe sites in *h*-*R*FeO$_3$. The four spin structures come from the combination of two ϕ angles and two relative alignments of the spins between the two FeO layers (parallel or antiparallel). Only Γ_2 allows for spontaneous magnetic polarizations.

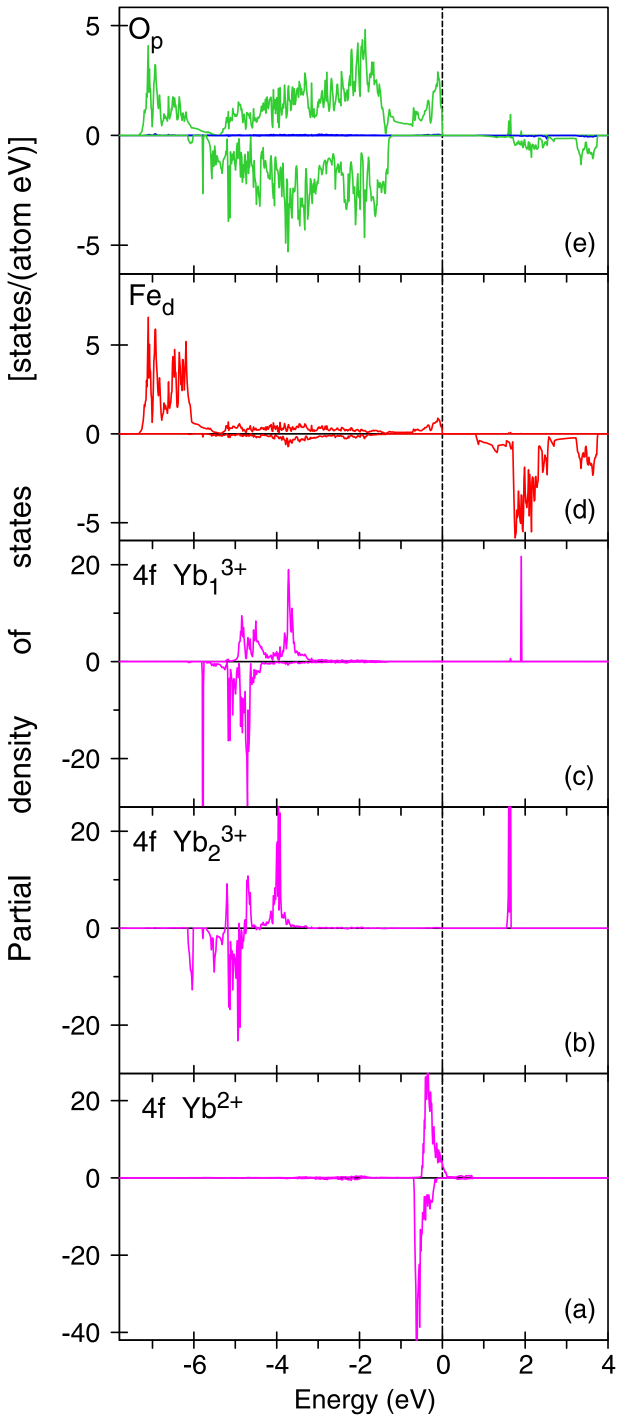

FIG. 3. The partial DOS of the *h*-YbFeO$_3$ calculated in the GGA+U approximation with $U_{\text{eff}} = 6.1$ and 3.3 eV for Yb and Fe, respectively.

on different Fe^{3+} sites. Mixing of Γ_2 with Γ_3 is also unlikely because it involves antiphase rotations of spins on different layers of Fe^{3+} sites which affect the interlayer couplings of the spins [32]. Therefore the magnetic structure has to include Γ_2 mixed with Γ_1, which contribute to the magnetic diffraction near (100) [32,61]. Our first principle calculations of spiral magnetic structures presented in Fig. 2 show quit small difference in total energy between these magnetic structures. The ground state corresponds to the Γ_2 configuration.

The rotation of FeO$_5$ due to structure distortion below 1000 K and canting Fe spin moments produces a small projection of the Fe moment along the c axis of around 0.05 ± 0.01 μ_{B}/f.u. on top of a 120° antiferromagnetic order below about 120 K [31,34,35]. The Yb-Fe interaction is weaker but sufficient enough to partially align the moment on Yb and contribute to the total magnetization. The magnetization of Fe is antiparallel to the magnetic field and to that of the Yb magnetization at low temperature. This provides a direct observation of ferrimagnetic order in the *h*-YbFeO$_3$.

Figure 3 presents the partial DOS of the *h*-YbFeO$_3$ calculated in the GGA+U approximation. We found two independent solutions in the *h*-YbFeO$_3$ with divalent Yb^{2+} and trivalent Yb^{3+} ions. The divalent Yb ion solution can be obtained only with fixed Yb $4f^{14}$ occupation number. This solution is not stable due to pinning of the Yb $4f$ states at the Fermi level [Fig. 3(a)]. It has small spin magnetic moment at the Yb site of around 0.244 μ_{B} and $4f$ occupation $n_{4f} = 13.75$. The self-consistent solution with relaxed Yb $4f$ occupation leads to the trivalent states at the Yb sites. It is in agreement with the experimental observations. Cao *et al.* [31] argue that Yb is in trivalent state in the *h*-YbFeO$_3$. They found an indication of Yb^{2+} at the surface of samples grown in an Ar environment, suggesting an insignificant effect on the bulk magnetism of the *h*-YbFeO$_3$. For the trivalent Yb^{3+} solution [Fig. 3(b)], thirteen $4f$ electron bands are situated well below the Fermi level in the energy range between −4.4

and −6.9 eV. Single hole level is situated far above the Fermi level. Actually, there are two empty $4f$ hole peaks above the Fermi level due to slightly different crystallographic positions of the Yb_1 and Yb_2 ions. The Yb $4f^{3+}$ energy bands are split due to the spin-orbit (SO) coupling ($\Delta\epsilon_{\mathrm{so}} = 1.5$ eV) as well as the Zeeman effect and separated from the $4f$ hole state by the correlation energy U_{eff}. The position of occupied $4f$ bands in the h-YbFeO$_3$ is in good agreement with x-ray photoemission measurements [31]. The Yb^{3+} spin and orbital magnetic moments are equal to $M_{\mathrm{spin}} = 0.36\ \mu_{\mathrm{B}}$ and $M_{\mathrm{orbit}} = 1.07\ \mu_{\mathrm{B}}$. It gives the value of total magnetic moment of $1.43\ \mu_{\mathrm{B}}$ in good agreement with the experimental value of $1.6\ \mu_{\mathrm{B}}$ from Cao *et al.* [31] and $1.5\ \mu_{\mathrm{B}}$ from Iida *et al.* [26]. We should mention that for the Yb^{3+} solution $M_{\mathrm{orbit}}/M_{\mathrm{spin}} = 2.92$ which is very close to the pure $J = 7/2, L = 3, S = 1/2$ multiplet for which $M_{\mathrm{orbit}}/M_{\mathrm{spin}} = 3$. This indicates that admixture from other multiplets such as $J = 5/2$ are very small.

Comparing the Fe $3d$ and O $2p$ partial DOS presented in Figs. 3(d) and 3(e), respectively, we can conclude strong Fe $3d$- O $2p$ hybridization. The Fe spin and orbital magnetic moments are equal to $3.738\ \mu_{\mathrm{B}}$ and $0.048\ \mu_{\mathrm{B}}$, respectively. It gives the value of total magnetic moment of $3.785\ \mu_{\mathrm{B}}$.

IV. X-RAY ABSORPTION AND XMCD SPECTRA

A. Yb $M_{4,5}$ x-ray absorption and XMCD spectra

Figure 4 presents the experimentally measured [31] (magenta circles) and theoretically calculated (full blue curves) XAS (the upper panel) and XMCD spectra of the h-YbFeO$_3$ at the Yb $M_{4,5}$ edges. Two peaks are observed in the x-ray absorption spectra at approximately 1513 and 1555 eV, which can be assigned to M_5 and M_4 excitations, respectively, according to the photon energy [62]. The experimentally measured XAS at the M_5 edge consists of a simple nearly symmetric peak that has no distinct structure. The XAS at the M_4 edge has much smaller intensity in comparison with the M_5 one.

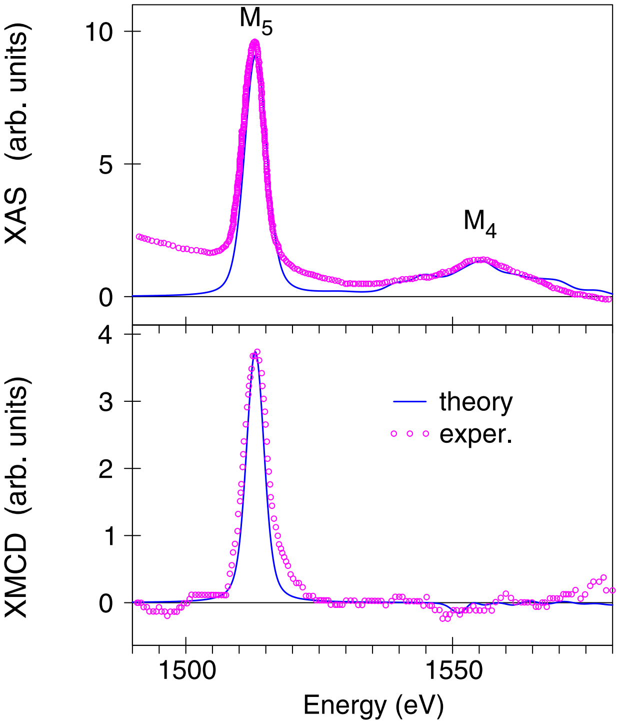

FIG. 4. Experimentally measured [31] (magenta circles) and theoretically calculated (full blue curves) XAS (top) and XMCD spectra at the Yb $M_{4,5}$ edges.

We recall that the M_4 (M_5) edge corresponds to $3d_{3/2}(3d_{5/2}) \rightarrow 4f$ transitions. The created $3d$ core hole has electrostatic interaction with the $4f$ shell. However, in a first approximation, this interaction can be neglected since no clear multiplet structure is distinguished in the measured absorption spectra. This approximation is supported theoretically since the Slater integrals $F_k(3d,4f)$ and $G_k(3d,4f)$ are small compared to the $F_k(4f,4f)$ integrals and $3d$ spin-orbit interaction [63]. Neglecting the core-level splitting the measured spectra reflect the density of states above the Fermi level weighted by the dipole transition probabilities. Because of the electric dipole selection rules ($\Delta l = \pm 1$; $\Delta j = 0, \pm 1$) the major contribution to the absorption at the M_4 edge stems from the transitions $3d_{3/2} \rightarrow 4f_{5/2}$ and that at the M_5 edge originates primarily from $3d_{5/2} \rightarrow 4f_{7/2}$ transitions, with a weaker contribution from $3d_{5/2} \rightarrow 4f_{5/2}$ transitions. For the later case, the corresponding $3d_{5/2} \rightarrow 4f_{5/2}$ radial matrix elements are only slightly smaller than for the $3d_{5/2} \rightarrow 4f_{7/2}$ transitions. The angular matrix elements, however, strongly suppress the $3d_{5/2} \rightarrow 4f_{5/2}$ contribution. Therefore the contribution to XAS spectrum at the M_5 edge from the transitions with $\Delta j = 0$ is about 15 times smaller than the transitions with $\Delta j = 1$ [39].

The hole state is completely empty and has almost pure $4f_{7/2}$ character. One can note, however, that the crystal-field splitting and the Yb $4f$-O $2p$ hybridization reduce the symmetry of the hole electronic state. It has also the $4f_{5/2}$ character, however, the latter contribution is almost two order of magnitude smaller than the $4f_{7/2}$ one. Therefore the M_4 peak is rather weak in comparison with the M_5 one but still has nonzero intensity.

The experimentally measured dichroic M_5 line in the h-YbFeO$_3$ consists of a simple nearly symmetric positive peak that has no distinct structure. The dichroic line at the M_4 edge has intensity on the level of the experimental errors. The selection rules for the magnetic quantum number m_j (m_j is restricted to $-j, \ldots, +j$) are $\Delta m_j = +1$ for $\lambda = +1$ and $\Delta m_j = -1$ for $\lambda = -1$. Table I presents the dipole allowed transitions for x-ray absorption spectra at the M_5 and M_4 edges for left ($\lambda = +1$) and right ($\lambda = -1$) polarized x rays.

To go further, we needs to discuss the characteristic of the $4f$ empty states. Since l and s prefer to couple parallel for more than half-filled shells, the $j = l - s = 5/2$ has a lower energy than the $j = l + s = 7/2$ level. Due to the intra-atomic exchange interaction the lowest sublevel of the $j = 5/2$ will be $m_{5/2} = +5/2$, however, for the $j = 7/2$, the lowest sublevel will be $m_{7/2} = -7/2$. This reversal in the energy sequence arises from the gain in energy due to alignment of the spin with the exchange field [64]. The hole state with almost pure $4f_{7/2}$ character has $m_j = -1/2$ and $+5/2$ occupations. Small amount of the $4f_{5/2}$ states mixed with the $4f_{7/2}$ has j projections $m_j = +1/2$ and $-5/2$.

Therefore, for the M_5 XMCD spectrum from the transitions listed in Table I, the dipole allowed transitions for $\lambda = +1$

TABLE I. The dipole allowed transitions from core $3d_{3/2,5/2}$ levels to the unoccupied $4f_{5/2,7/2}$ valence states for left ($\lambda = +1$) and right ($\lambda = -1$) polarized x rays.

Edge	$\lambda = +1$	$\lambda = -1$
M_5	$-5/2 \to -3/2$	$-5/2 \to -7/2$
	$-3/2 \to -1/2$	$-3/2 \to -5/2$
	$-1/2 \to +1/2$	$-1/2 \to -3/2$
	$+1/2 \to +3/2$	$+1/2 \to -1/2$
	$+3/2 \to +5/2$	$+3/2 \to +1/2$
	$+5/2 \to +7/2$	$+5/2 \to +3/2$
M_4	$-3/2 \to -1/2$	$-3/2 \to -5/2$
	$-1/2 \to +1/2$	$-1/2 \to -3/2$
	$+1/2 \to +3/2$	$+1/2 \to -1/2$
	$+3/2 \to +5/2$	$+3/2 \to +1/2$

are $-3/2 \to -1/2$ and $+3/2 \to +5/2$ and those for $\lambda = -1$ are $+1/2 \to -1/2$. The transitions with the same final states $m_j = -1/2$ mostly cancel each other. Thus the XMCD spectrum of the h-YbFeO$_3$ at the M_5 edge can be roughly approximated by the $N^{7/2}_{5/2}$ m_j projected partial densities of states. Here we use the notation $N^{j}_{m_j}$ for the density of states with the total momentum j and its projection m_j. This explains why the dichroic M_5 line in the h-YbFeO$_3$ consists of a single nearly symmetric peak.

For the M_4 XMCD spectrum, the dipole allowed transitions for $\lambda = +1$ are $-1/2 \to +1/2$ and those for $\lambda = -1$ are $-3/2 \to -5/2$ and $+3/2 \to +1/2$. The transitions with the same final states $m_j = +1/2$ mostly cancel each other. Thus the XMCD spectrum of the h-YbFeO$_3$ at the M_4 edge can be approximated by the $-N^{5/2}_{5/2}$ partial densities of states. Therefore the dichroic M_4 line in the h-YbFeO$_3$ also consists of a single nearly symmetric peak with opposite sign to the M_5 XMCD spectrum. The occupation number of the $m^{5/2}_{5/2}$ is almost two order of magnitude smaller than the $m^{7/2}_{5/2}$ one. As a result, the intensity of the M_4 XMCD spectrum is much smaller than the M_5 one (see the lower panel of Fig. 4).

We should note, however, that the explanation of the XMCD line shape in terms of m_j-projected DOS presented above should be considered as only qualitative. There is no full compensation between transitions with equal final states due to difference in the angular matrix elements. It is always difficult to estimate an appropriate atomic $4f$ occupation number in band-structure calculations. Such a determination is usually obtained by the integration of the $4f$ electron charge density inside of the corresponding atomic sphere. We, however, should keep in mind that some amount of the $4f$ states are derived from the so-called "tails" of Fe $3d$ states arising as a result of the decomposition of the wave function centered at Fe atoms.

B. Fe $L_{2,3}$ x-ray absorption and XMCD spectra

Figure 5 shows the calculated isotropic x-ray absorption and XMCD spectra of Fe at the $L_{2,3}$ edges in the GGA+U approach together with the experimental data [65]. Because of the dipole selection rules, apart from the $4s_{1/2}$ states (which have a small contribution to the XAS due to relatively small $2p \to 4s$ matrix elements) only $3d_{3/2}$ states occur as final states for L_2 XAS for unpolarized radiation, whereas for the L_3 XAS the $3d_{5/2}$ states also contribute [39]. Although the $2p_{3/2} \to 3d_{3/2}$ radial matrix elements are only slightly smaller than for the $2p_{3/2} \to 3d_{5/2}$ transitions, the angular matrix elements strongly suppress the $2p_{3/2} \to 3d_{3/2}$ contribution [39]. Therefore, neglecting the energy dependence of the radial matrix elements, the L_2 and the L_3 spectrum can be viewed as a direct mapping of the DOS curve for $3d_{3/2}$ and $3d_{5/2}$ character, respectively.

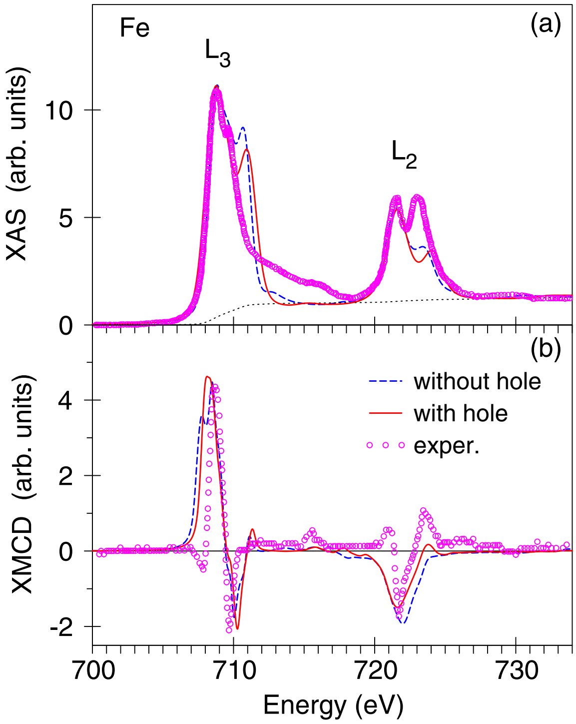

FIG. 5. (a) Experimentally measured [31] (circles) absorption spectrum of the h-YbFeO$_3$ at the Fe $L_{2,3}$ edges measured with circularly polarized counterclockwise x rays in a 10 kOe external field at 6.5 K in comparison with the theoretically calculated spectra without (dashed blue lines) and with taking into account core-hole effect (full red lines). Dotted black lines show the theoretically calculated background spectra; (b) experimental [31] (circles) XMCD spectra of the h-YbFeO$_3$ at the Fe $L_{2,3}$ edges in comparison with theoretically calculated ones without (dashed blue lines) and with taking into account core-hole effect (full red lines).

The GGA+U approach gives quite reasonable agreement with the experiment, except for slightly larger width of the Fe L_3 XAS in comparison with the experimental spectrum. Also we are not able to reproduce a low-energy negative peak at around 709 eV in the L_3 XMCD spectrum and high-energy positive peak at 724 eV at the L_2 edge. Note that for the GGA approach, the agreement between theoretically calculated and experimental XAS and XMCD spectra is much worse (not shown), which indicates on the correlated nature of the Fe electronic states in the h-YbFeO$_3$.

We investigate the core-hole effect in the final state using the supercell approximation. When the $2p$ core electron is photoexcited to the unoccupied $3d$ states, the distribution of the charge changes to account for the created hole. To check the convergence of XAS and XMCD spectra for the impurity site, we used supercell calculations with two and four formula units. Very similar spectra were obtained in both cases. The final-state interaction slightly improves the agreement between theoretically calculated and the experimental XMCD spectra at the $L_{2,3}$ edge, however, it has minor influence on the Fe $L_{2,3}$ XAS spectra.

C. O *K* x-ray absorption, XLD and XMCD spectra

The XAS and XMCD spectra in metals at the K edge where the 1s core electrons are excited to the p states through the dipolar transition usually attract only minor interest because p states are not the states that influence the magnetic and orbital orders. Recently, however, the understanding of p states has become important since XMCD spectroscopy using the K edges of transition metals and compounds became popular [39]. Because of the delocalized nature of p states, the K-edge XMCD is sensitive to the electronic structure of neighboring sites.

Cao *et al.* [31] measured the absorption spectra at the O K edge in h-YbFeO$_3$ using a linearly polarized x-rays. Figures 6(a) and 6(b) shows the theoretically calculated (full blue lines) and experimentally measured [31] (circles) absorption spectra for s (a) and p (b) of the h-YbFeO$_3$ at the O K edge. The panels (c) and (d) present theoretically calculated O K XLD and XMCD spectra, respectively. There is a significant difference between the spectra with an s-polarized x rays (E $\perp$ c) and that with a p-polarized x rays (E $\parallel$ c) consistent with the large structural anisotropy. Two peaks are observed in the absorption spectrum for an s-polarized x rays at approximately 533.5 and 538.5 eV with deep minimum in between [Fig. 6(b)]. There is also a high-energy shoulder at 540–542 eV. A p-polarized x rays produce two similar peaks at 533.5 and 539.5 eV but instead of deep minimum there is an additional peak in between these major peaks [Fig. 6(a)]. The theoretical calculations well reproduce the O K XAS spectra for both the polarizations.

The O K edge XAS spectra fundamentally reveal a transition from the O 1s core state to the unoccupied O 2p derived states, which are hybridized with the relatively narrow empty 3d bands and broader 4p bands of the Fe ions and very narrow Yb 4f band and quite broad Yb 5d bands. To clarify the nature of fine structures of the oxygen x-ray absorption spectra at the K edge, we present in Fig. 7 the oxygen empty 2p partial DOSs of the h-YbFeO$_3$ calculated in the GGA+U approximation. We present two types of oxygen ions, namely, oxygens in close vicinity of Fe ions, O$_{\mathrm{Fe}}$, and nearest oxygen neighbors of Yb ions, O$_{\mathrm{Yb}}$ (see Fig. 1). The 2p partial DOS of O$_{\mathrm{Fe}}$ and O$_{\mathrm{Yb}}$ ions have quite different shapes due to different hybridizations with neighbor atoms. There are two groups of the oxygen empty 2p states: from 0.7 to 3.8 eV and from 5.1 up to 9.7 eV for both the DOSs. These two groups are divided by the energy gap of approximately 1.3 eV. The empty Yb 5d states, presented in the lower panel of Fig. 7 by green curve, are very close in shape and intensity to the 2p states at the O$_{\mathrm{Yb}}$ oxygen sites due to strong O 2p - Yb 5d hybridization. On the other hand, the corresponding high-energy 2p states at the O$_{\mathrm{Fe}}$ sites are devoted to the O 2p - Fe 4p hybridization effect (the upper panel of Fig. 7). They have much smaller intensity in comparison with the oxygen 2p states at the O$_{\mathrm{Yb}}$ sites. The low-energy group of the oxygen partial DOS $N_{2p}(E)$ is due to the hybridization of the O 2p with Fe 3d and Yb 4f states. They have different shapes for these two groups of oxygen ions. The 2p spin-down O$_{\mathrm{Fe}}$ states are well hybridized with corresponding spin-down Fe 3d states [compare Fig. 3(d) and the upper panel of Fig. 7]. On the other hand, 2p spin-up O$_{\mathrm{Yb}}$ partial DOS has strong narrow double peak at around 1.6–1.9 eV due to the O 2p - Yb 4f hybridization. Such the peak is almost completely suppressed for the $N_{2p}(E)$ at the O$_{\mathrm{Fe}}$ sites.

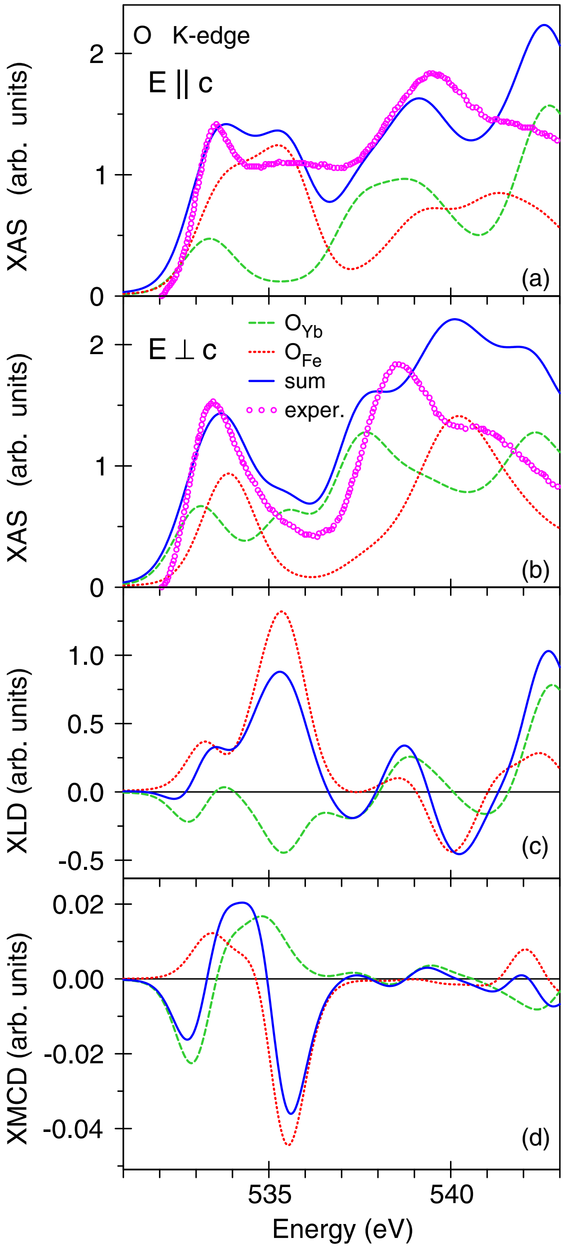

FIG. 6. Theoretically calculated (full line) and experimentally measured [31] (circles) absorption spectra measured using linearly polarized x rays for s (a) and p (b) of the h-YbFeO$_3$ at the O K edge. (c) and (d) present theoretical O K XLD and XMCD spectra, respectively. All the spectra are decomposed by partial contributions from the oxygen ions occupied the O$_{\mathrm{Fe}}$ (red dotted curves) and O$_{\mathrm{Yb}}$ (dashed green curves) sites.

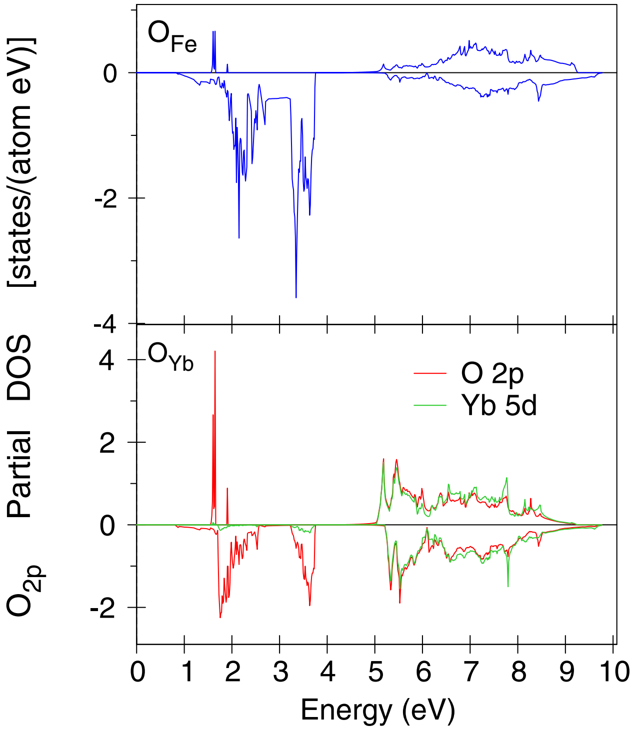

FIG. 7. The oxygen empty $2p$ partial DOSs of the h-YbFeO$_3$ calculated for oxygens in close vicinity of Fe ions (top) and nearest oxygen neighbors of Yb ions (bottom).

From analysis of the oxygen empty $2p$ partial DOS, we can conclude that the fine structures of the O K XAS spectra at 532 to 537 eV energy range are derived from the $1s$ states to the empty O $2p$ states situated at 1.5 to 4 eV above the Fermi level. The peaks above 537 eV reflect the energy distribution of the O $2p$ empty states between 5 and 10 eV above the Fermi level.

The panels (a) and (b) of Fig. 6 present also theoretical O K XAS spectra decomposed by partial contributions from the oxygen ions occupied the O$_{Fe}$ (red dotted curves) and O$_{Fe}$ (dashed green curves) sites. The low-energy fine structure of the O K XAS spectrum for the E $\parallel$ c polarization has two peaks. The low-energy peak is devoted to the $1s \rightarrow O_{2p}^{Yb}$ transitions and the high-energy peak is due to the $1s \rightarrow O_{2p}^{Fe}$ transitions. The corresponding fine low-energy structure for the E $\perp$ c hybridization has only one peak structure at 533.5 eV because the energy shift between corresponding peaks in the $N_{2p}(E)$ partial DOS for the O$_{Fe}$ and O$_{Fe}$ sites is much smaller in comparison with the E $\parallel$ c polarization.

Figure 6(c) presents theoretical O K XLD spectrum decomposed by partial contributions from the oxygen ions occupied the O$_{Fe}$ (red dotted curves) and O$_{Fe}$ (dashed green curves) sites. We found that the contributions from these two different sites are quite different in the shape and amplitude.

The panel (d) of Fig. 6 presents theoretically calculated O K XMCD spectrum. Due to strong hybridization of the O $2p$ states with the Fe $3d$ and Yb ($4f$, $5d$) states, oxygen ions possess relatively large spin magnetic moments ranging from 0.107 μ_B for the O$_{Yb}$ ions to 0.371 μ_B for O$_{Fe}$ ones. Orbital moments were found to be equal to 0.001 for the O$_{Yb}$ ions and 0.002 μ_B for O$_{Fe}$ μ_B ones. Despite these small orbital moments there is quite pronounced dichroism at the oxygen K edge, however, it is still one order of magnitude smaller than the corresponding XLD spectrum. There are two negative minima at 533 and 535.5 eV and positive structure between 533.5 and 534.5 eV. The contributions from the O$_{Fe}$ and O$_{Fe}$ sites are also different in the shape and amplitude.

V. CONCLUSIONS

The electronic and magnetic structures and x-ray magnetic circular dichroism of the h-YbFeO$_3$ were investigated theoretically within a DFT-GGA approach in the framework of the fully relativistic spin-polarized Dirac LMTO band-structure method with consideration of Coulomb electron-electron correlations. The $4f$ electrons of Yb are explicitly treated as valence electrons.

The Coulomb repulsion $U_{\rm eff}$ strongly influences the electronic structure of the h-YbFeO$_3$. GGA+U theory predicts that the ytterbium ions in the h-YbFeO$_3$ are in trivalent state. For Yb^{3+} ions, thirteen $4f$ bands are fully occupied and hybridize with oxygen $2p$ and Fe $3d$ states. The Yb $4f$ hole level is completely unoccupied and well above the Fermi level. It has almost pure $4f_{7/2}$ character. However, the crystal-field splitting and the Yb $4f$ - O $2p$ hybridization reduce the symmetry of the hole electronic state. It has also the $4f_{5/2}$ character, but the latter contribution is almost two order of magnitude smaller than the $4f_{7/2}$ one. The Yb^{3+} spin and orbital magnetic moments are equal to 0.36 μ_B and 1.07 μ_B, respectively. It gives the value of total magnetic moment of 1.43 μ_B. The magnetization of Fe and Yb along the c axis are antialigned.

The x-ray absorption spectra, XLD and XMCD spectra at the Yb $M_{4,5}$, Fe $L_{2,3}$, and O K edges were investigated theoretically. The calculated results are in good agreement with experimental data. A qualitative explanation of the XMCD spectra is provided by the analysis of the corresponding selection rules, orbital character and occupation numbers of individual $4f$ orbitals. The hole states with almost pure $4f_{7/2}$ character have $m_j = -1/2$ and $+5/2$ occupations. Small amount of the $4f_{5/2}$ states have $m_j = +1/2$ and $-5/2$. The XMCD spectra at the Yb M_5 and M_4 edges can be roughly approximated by the $N_{5/2}^{7/2}$ and $-N_{5/2}^{5/2}$ projected partial densities of states, respectively. As a result, the shapes of both the Yb M_5 and M_4 XMCD spectra contain single nearly symmetric peak with opposite signs. The occupation number of the $m_{5/2}^{5/2}$ is almost two order of magnitude than the $m_{5/2}^{7/2}$ one. As a result, the intensity of the M_4 XMCD spectrum is much smaller than the M_5 one.

The past decade has witnessed dramatic progress in the fundamental physics of multiferroics and magnetoelectrics. The challenge and opportunity for solid-state physicists is to identify mechanisms that provide large, robust, and coupled magnetization and polarization, combined with large susceptibilities at low electric or magnetic fields, all at room temperature. Multiferroics continue to reveal novel, unanticipated physics, and the potential applications now stretch far beyond electrical control of ferromagnetism. We hope that the recent progress on the basic materials physics aspects will stimulate the physics community to dream up entirely new device paradigms that exploit the novel and unique functionalities of multiferroics.

ACKNOWLEDGMENTS

V.N.A. gratefully acknowledges the hospitality at the Faculty of Mathematics and Informatics of the University of Bialystok during his stay there. D.A.K. gratefully acknowledges the hospitality at the Max-Planck-Institut für Festkörperforschung in Stuttgart during his stay there. The studies were supported by the National Academy of Sciences of Ukraine within the budget program KPKBK 6541230-1A “Support for the development of priority areas of scientific research.”

---

[1] K. Aizu, Phys. Rev. B **2**, 754 (1970).
[2] N. A. Spaldin and M. Fiebig, Science **309**, 391 (2005).
[3] W. Eerenstein, N. D. Mathur, and J. F. Scott, Nature (London) **442**, 759 (2008).
[4] C. Binek and B. Doudin, J. Phys.: Condens. Matter **17**, L39 (2005).
[5] M. Gajek, M. Bibes, S. Fusil, K. Bouzehouane, J. Fontcuberta, A. Barthelemy, and A. Fert, Nat. Mater. **6**, 296 (2007).
[6] C.-W. Nan, M.-I. Bichurin, S. Dong, D. Viehland, and G. Srinivasan, J. Appl. Phys. **103**, 031101 (2008).
[7] J. Wang, J. B. Neaton, H. Zheng, V. Nagarajan, S. B. Ogale, B. Liu, D. Viehland, V. Vaithyanathan, D. G. Schlom, U. V. Waghmare *et al.*, Science **299**, 1719 (2003).
[8] A. Stroppa, M. Marsman, G. Kresse, and S. Picozzi, New J. Phys. **12**, 093026 (2010).
[9] A. Kimel, A. Kirilyuk, A. Tsvetkov, R. Pisarev, and T. Rasing, Nature (London) **429**, 850 (2004).
[10] J. A. de Jong, A. V. Kimel, R. V. Pisarev, A. Kirilyuk, and T. Rasing, Phys. Rev. B **84**, 104421 (2011).
[11] R. L. White, J. Appl. Phys. **40**, 1061 (1969).
[12] R. M. Bozorth, V. Kramer, and J. P. Remeika, Phys. Rev. Lett. **1**, 3 (1958).
[13] Y. B. Bazaliy, L. T. Tsymbal, G. N. Kakazei, V. I. Kamenev, and P. E. Wigen, Phys. Rev. B **72**, 174403 (2005).
[14] M. Marezio, J. P. Remeika, and P. D. DerNier, Acta Crystallogr., Sect. B **26**, 300 (1970).
[15] M. A. Pena and J. L. G. Fierro, Chem. Rev. **101**, 1981 (2001).
[16] E. Magome, C. Moriyoshi, Y. Kuroiwa, A. Masuno, and H. Inoue, Jpn. J. Appl. Phys. **49**, 09ME06 (2010).
[17] J. A. Kurzman, J. Li, T. D. Schladt, C. R. Parra, X. Ouyang, R. Davis, J. T. Miller, S. L. Scott, and R. Seshadri, Inorg. Chem. **50**, 8073 (2011).
[18] S. Zhou, S. Mao, Z. Xie, and L. Zheng, Sens. Actuators B **156**, 23 (2011).
[19] H. Han, D. Kim, K. Chu, J. Park, S. Y. Nam, S. Heo, C.-H. Yang, and H. M. Jang, Appl. Mater. Interfaces **10**, 1846 (2018).
[20] T. Nishimura, S. Hosokawa, Y. Masuda, K. Wada, and M. Inoue, J. Solid State Chem. **197**, 402 (2013).
[21] C. J. Fennie and K. M. Rabe, Phys. Rev. B **72**, 100103 (2005).
[22] A. Muñoz, J. A. Alonso, M. J. Martínez-Lope, M. T. Casáis, J. L. Martínez, and M. T. Fernández-Díaz, Phys. Rev. B **62**, 9498 (2000).
[23] W. Wang, H. Wang, X. Xu, L. Zhu, L. He, E. Wills, X. Cheng, D. J. Keavney, J. Shen, X. Wu *et al.*, Appl. Phys. Lett. **101**, 241907 (2012).
[24] M. Fiebig, D. Frohlich, K. Kohn, S. Leute, T. Lottermoser, V. V. Pavlov, and R. V. Pisarev, Phys. Rev. Lett. **84**, 5620 (2000).
[25] Y. K. Jeong, J.-H. Lee, S.-J. Ahn, S.-W. Song, H. M. Jang, H. Choi, and J. F. Scott, J. Am. Chem. Soc. **134**, 1450 (2012).
[26] H. Iida, T. Koizumi, Y. Uesu, K. Kohn, N. Ikedai, S. Mori, R. Haumont, P.-E. Janolin, J.-M. Kiat, M. Fukunaga *et al.*, J. Phys. Soc. Jpn. **81**, 024719 (2012).
[27] M. Iglesias, A. Rodríguez, P. Blaha, V. Pardo, D. Baldomir, M. Pereiro, J. Botana, J. E. Arias, and K. Schwarz, J. Magn. Magn. Mater. **290-291**, 396 (2005).
[28] B.-L. Xing, L. Wu, G.-P. Qin, Y. Li, Y.-F. Zhang, and J.-Q. Li, Acta Chim. Sin. **65**, 1773 (2007).
[29] D. J. Adams and B. Amadon, Phys. Rev. B **79**, 115114 (2009).
[30] S. E. Nikitin, L. S. Wu, A. S. Sefat, K. A. Shaykhutdinov, Z. Lu, S. Meng, E. V. Pomjakushina, K. Conder, G. Ehlers, M. D. Lumsden *et al.*, Phys. Rev. B **98**, 064424 (2018).
[31] S. Cao, K. Sinha, X. Zhang, X. Zhang, X. Wang, Y. Yin, A. T. N’Diaye, J. Wang, D. J. Keavney, T. R. Paudel *et al.*, Phys. Rev. B **95**, 224428 (2017).
[32] W. Wang, J. Zhao, W. Wang, Z. Gai, N. Balke, M. Chi, H. N. Lee, W. Tian, L. Zhu, X. Cheng *et al.*, Phys. Rev. Lett. **110**, 237601 (2013).
[33] S. M. Disseler, J. A. Borchers, C. M. Brooks, J. A. Mundy, J. A. Moyer, D. A. Hillsberry, E. L. Thies, D. A. Tenne, J. Heron, M. E. Holtz *et al.*, Phys. Rev. Lett. **114**, 217602 (2015).
[34] H. Das, A. L. Wysocki, Y. Geng, W. Wu, and C. J. Fennie, Nat. Commun. **5**, 2998 (2014).
[35] S. Cao, X. Zhang, T. R. Paudel, K. Sinha, X. Wang, X. Jiang, W. Wang, S. Brutsche, J. Wang, P. J. Ryan *et al.*, J. Phys.: Condens. Matter **28**, 156001 (2016).
[36] D. J. Downie, R. J. Goff, W. Kockelmann, S. D. Forder, J. E. Parker, F. D. Morrison, and P. Lightfoot, J. Solid State Chem. **190**, 52 (2012).
[37] X. Xu and W. Wang, Mod. Phys. Lett. **28**, 1430008 (2014).
[38] G. Y. Guo, H. Ebert, W. M. Temmerman, and P. J. Durham, Phys. Rev. B **50**, 3861 (1994).
[39] V. Antonov, B. Harmon, and A. Yaresko, *Electronic Structure and Magneto-Optical Properties of Solids* (Kluwer, Dordrecht, 2004).
[40] E. Arola, M. Horne, P. Strange, H. Winter, Z. Szotek, and W. M. Temmerman, Phys. Rev. B **70**, 235127 (2004).
[41] V. N. Antonov, O. Jepsen, A. N. Yaresko, and A. P. Shpak, J. Appl. Phys. **100**, 043711 (2006).
[42] V. N. Antonov, B. N. Harmon, A. N. Yaresko, and A. P. Shpak, Phys. Rev. B **75**, 184422 (2007).

[43] V. N. Antonov, A. N. Yaresko, and O. Jepsen, Phys. Rev. B **81**, 075209 (2010).
[44] O. K. Andersen, Phys. Rev. B **12**, 3060 (1975).
[45] V. V. Nemoshkalenko, A. E. Krasovskii, V. N. Antonov, V. N. Antonov, U. Fleck, H. Wonn, and P. Ziesche, Phys. status solidi B **120**, 283 (1983).
[46] J. P. Perdew, K. Burke, and M. Ernzerhof, Phys. Rev. Lett. **77**, 3865 (1996).
[47] P. E. Blöchl, O. Jepsen, and O. K. Andersen, Phys. Rev. B **49**, 16223 (1994).
[48] A. N. Yaresko, V. N. Antonov, and P. Fulde, Phys. Rev. B **67**, 155103 (2003).
[49] V. I. Anisimov and O. Gunnarsson, Phys. Rev. B **43**, 7570 (1991).
[50] I. V. Solovyev, P. H. Dederichs, and V. I. Anisimov, Phys. Rev. B **50**, 16861 (1994).
[51] P. H. Dederichs, S. Blügel, R. Zeller, and H. Akai, Phys. Rev. Lett. **53**, 2512 (1984).
[52] W. E. Pickett, S. C. Erwin, and E. C. Ethridge, Phys. Rev. B **58**, 1201 (1998).
[53] M. Cococcioni and S. de Gironcoli, Phys. Rev. B **71**, 035105 (2005).
[54] K. Nakamura, R. Arita, Y. Yoshimoto, and S. Tsuneyuki, Phys. Rev. B **74**, 235113 (2006).
[55] F. Aryasetiawan, M. Imada, A. Georges, G. Kotliar, S. Biermann, and A. I. Lichtenstein, Phys. Rev. B **70**, 195104 (2004).
[56] I. V. Solovyev and M. Imada, Phys. Rev. B **71**, 045103 (2005).
[57] V. P. Antropov, V. N. Antonov, L. V. Bekenov, A. Kutepov, and G. Kotliar, Phys. Rev. B **90**, 054404 (2014).
[58] F. Aryasetiawan, K. Karlsson, O. Jepsen, and U. Schonberger, Phys. Rev. B **74**, 125106 (2006).
[59] J. L. Campbell and T. Parr, At. Data Nucl. Data Tables **77**, 1 (2001).
[60] A. A. Bossak, I. E. Graboy, O. Y. Gorbenko, A. R. Kaul, M. S. Kartavtseva, V. L. Svetchnikov, and H. W. Zandbergen, Chem. Mater. **16**, 1751 (2004).
[61] J. S. Helton, D. K. Singh, H. S. Nair, and S. Elizabeth, Phys. Rev. B **84**, 064434 (2011).
[62] J. A. Bearden, Rev. Mod. Phys. **39**, 78 (1967).
[63] S. P. Collins, D. Laundy, C. C. Tang, and G. van der Laan, J. Phys.: Condens. Matter **7**, 9325 (1995).
[64] P. Dalmas de Réotier, A. Yaouanc, G. van der Laan, N. Kernavanois, J.-P. Sanchez, J. L. Smith, A. Hiess, A. Huxley, and A. Rogalev, Phys. Rev. B **60**, 10606 (1999).
[65] A. Delobbe, A.-M. Dias, M. Finazzi, L. Stichauer, J.-P. Kappler, and G. Krill, Europhys. Lett. **43**, 320 (1998).